

Effect of crossflow velocity on underwater bubble swarms

Yang Xu¹, Aliyu Musa Aliyu², Hyunduk Seo², Jin-Jun Wang¹, Kyung Chun Kim^{2*}

¹ Key Laboratory of Fluid Mechanics, Beijing University of Aeronautics and Astronautics, Ministry of Education, Beijing 100191, China

²School of Mechanical Engineering, Pusan National University, 609-735, Busan, Republic of Korea

Abstract

We investigate the effect of crossflow velocity on submerged bubble plumes or swarms by employing the use of high-speed photography and an image-processing method to measure bubble rise velocities. Particle image velocimetry (PIV) was used to accurately determine the crossflow freestream velocity as well as boundary layer information. We varied the gas flow rates from 2 to 25 L/min. This range exceeds those of previous studies we could find in the open literature which were mostly less than 5 L/min and involved isolated bubbles. Combined with the crossflow velocities, this resulted in the investigation of a wide range of flow conditions providing a database of 36 experimental data points and constitutes a substantial addition to the bubble swarm/crossflow literature. Because our experiments involved larger gas flow rates than previously reported, we had to develop a digital image-processing algorithm using standard functions in Matlab to measure swarm rise velocities, and angles of inclination under crossflow. Results were validated against reported data at similar experimental conditions. It was established that increasing freestream velocity strongly suppressed bubble rise velocities and resulted in bubble breakup. Relationships for predicting rise velocity and inclination angle were derived as non-dimensional functions of the crossflow velocity, fluid properties and inlet gas flow rates. These showed good agreement with the current as well as reported experimental data.

Keywords: Bubbly flow, bubble swarms, bubble trajectory, crossflow, visualization

1 Introduction

Gas dispersion by under-liquid injection from submerged orifices is a useful operation in many industrial processes. These include wastewater treatment, absorption towers, aerated stirred tanks, metallurgical smelting and biological processes such as nitrification, and microorganism metabolism. In these applications, the gas–liquid interfacial surface area per unit volume is an important parameter that determines heat, concentration and mass transfer rates. It has been reported that smaller bubbles (and hence increased interfacial area) are created by having the continuous phase to flow normally across the path of the emerging gas bubbles [1]–[5]. Such crossflows allow bubble ejection frequency to be controlled and they ensure that detached bubbles are likely to be swept away from the region of the nozzle, thus reducing the likelihood of coalescence [3], [4]. Forrester & Rielly [5] noted that drag force created by the flowing liquid and increased boundary layer transport are responsible for the

generation of smaller bubbles as well as their rapid detachment from the orifice. The bubble's rise velocity as well as trajectory are now affected by the momentum of the liquid crossflow. In addition to the buoyancy, virtual mass, surface tension, and inherent drag forces the bubbles experience in liquid, there is an additional drag force normal to the plane of the rising bubbles and this greatly impacts the bubbles rising profile as there is now a horizontal component.

Manasseh et al. [6] studied the effect of liquid crossflows on bubble trajectory for single bubbles as well as for bubble swarms. They noticed that bubbling rate increased with increasing continuous phase crossflow velocity and the formation of trajectory bifurcations (when viewed from above) at high crossflow velocities. However, their study did not consider the effect of crossflow velocity on the bubble rise velocities. Socolofsky & Adams [7] investigated bubble swarms (referred to as plumes in their work) under liquid crossflow in a flow channel using air as the dispersed phase and oil and alcohol as the continuous phases. Using an organic dye in the continuous phase, a characterisation of the various bubble regions of the swarm were carried out and were categorised as "separation", "mixed plume", "buoyant jet" and "fractionation" regions. An empirical correlation was derived via dimensional analysis relating the freestream velocity with the critical separation height, defined as the height when horizontal motion strips entrained fluid away from the dispersed phase. They argued that this separation height causes a stratification of the bubbly flow under crossflow and is important in the study of deep-sea blowouts of oil and gas. Nevertheless, their study also did not examine the effect of the crossflow on the swarm rise velocities.

An experimental investigation was carried out by Zhang & Zhu [8] on the effect of water crossflow on an air/water two-phase bubbly jet. A key feature of this study was that pure air injection (i.e. a bubbly plume or swarm) was not done but premixed air/water (a bubbly jet) using a Venturi ejector and then through nozzle to the freestream. Their air flow rates at the nozzle used in their experiments were 1, 3 and 5 L/min. Void fraction was measured using a computer-controlled optical fibre probe inclinable according to the angle of the jet. Dye premixed with the incoming water was used to visualise the different trajectories assumed by the bubbles from the liquid crossflow indicating a phase slip. The optical fibre probe was double tipped, as such, signals obtained from both sensors were cross-correlated to determine bubble velocity profiles at different heights. From this study, Zhang & Zhu [8] established that with the air/water jet and crossflow, bubble size was more uniform than in the quiescent liquid condition and their interfacial area followed a Gaussian distribution. They also found that bubble property values decay along the gas-phase centreline trajectory until they terminal values are attained. An empirical relationship for void fraction was proposed to describe such a trend. More importantly, they established that bubble induced water velocity inside the gas phase is substantial and was caused mainly by the passage of bubble clusters. But in the case of bubbly jets with large water superficial Reynolds numbers, induced water velocity is negligible, meaning the overriding controlling phase is

the water crossflow. However, their study significantly differs from the current one since two-phase air/water rather than single phase gas injection was done. Their case is more common in environmental conditions where wet gas blowouts occur either in underwater pipe bursts or from natural gas reservoirs. Single phase gas injection into bulk liquids is however common in industrial processing where their contacting is used to promote heat, mass, and concentration transfer. Furthermore, while the use of an optical fibre probe in determining bubble velocity, void fraction, and bubble size, offers a very fast method of measurement, it is rather intrusive especially in high Reynolds number crossflow conditions. For many bubbles the probe does not penetrate diametrically, and as such, bubble size can be grossly underestimated. Another drawback in using optical fibre probes is their fragility for high Reynolds number flows, and the complication involved in their manufacture since bespoke sensors have to be manually fabricated for specific channel geometries.

Unlike low Reynolds number single bubbles, rigorous theoretical treatment of bubble swarm properties is difficult due to intense turbulence. However, attempts have been made in the past at using numerical methods such as integral models [9]–[12]. Computational fluid dynamics (CFD) has also been used, such as the simulations using the k-epsilon turbulence model [13], large eddy simulations [14], and direct numerical simulations [15], [16]. Zhang & Zhu [8] noted that the main shortcoming with numerical simulation is the lack of full understanding of bubble–bubble and bubble–liquid interaction mechanisms, as well as bubble breakup and coalescence and bubble deformation mechanisms.

Here, we investigate the effect of crossflow velocity on submerged bubble swarms with a high gas flow rate and crossflow velocity than has been previously reported. A high-speed image-processing method was used to measure ejected bubble swarm properties. Particle image velocimetry (PIV) was used to accurately measure the crossflow freestream velocity as well as boundary layer information. We varied the gas flow rate and the values investigated were 2, 5, 10, 15, 20, and 25 L/min. This range exceeds those of previous studies in the open literature on bubble swarms which were mostly within the range of 1–5 L/min. Air injection flow rates were between 0.03–0.9 L/min resulting in single bubbles ejected at steady frequencies. However, these conditions are far from those found in industrial applications. Due to the comparatively large gas flow rates involved in the current study, it is more suited to conditions found in field conditions. As a result, a custom digital image-processing algorithm was developed to measure bubble rise velocities, trajectories, and size distribution in contact with the crossflow. Mean bubble sizes and rise velocities were determined and are correlated using the dominant dimensionless numbers. Comparisons are made with previous data and models and improved correlations were obtained for the inclination angle (trajectory) as well as the rise velocity.

2 Experimental setup and image processing

2.1 Experimental facility

The present experiment was conducted in a low-speed recirculating water channel with the working section of 3000 mm × 600 mm × 700 mm (length × width × height) in Beihang University. The water channel is made of smooth reinforced glass for full optical access to the flow inside. The free-stream velocity U_∞ could be adjusted up to 500 mm/s by a digital motor controller and the free-stream turbulence intensity is less than 0.5 %. For the current experiment, five free-stream velocities in the range of 58.5 mm/s ~ 334 mm/s, were tested for comparison. Figure 1 (a) presented the schematic diagram of the facility for bubble experiment. A flat plate with dimensions of 1500 mm × 500 mm × 10 mm (length × width × thickness) was horizontally positioned in the water channel with upper surface 520 mm below the free surface and lower surface 50 mm above the channel bottom. The flat plate has an 8:1 elliptical leading edge to prevent flow separation. A circular brass nozzle was set vertically in the middle of the flat plate to inject air into water. The nozzle exit, with an outer diameter (D_o) of 8.0 mm and inner diameter (d_{noz}) of 5.0 mm, was 28 mm above the flat plate, and its centreline was 760 mm away from the leading edge of the flat plate, as shown in Figure 1 (b). The air was supplied from a commercial air compressor with a capacity to deliver up to 7.0 bar pressure at constant flow rates. A manual valve together with a rotameter were set inline to control the air discharge and measure the flow rate. Moreover, in order to improve the accuracy of the flow rate measurement, a rotameter was specially chosen to ensure that the measured value was located between 40% and 70% of the maximum that could measure. This was the optimal measuring range for rotameters. In this study, the air flow rate (Q_g) was set as 2, 5, 10, 15, 20 and 25 L/min, corresponding to the air injecting velocity (u_g) equalling 1.7, 4.25, 8.5, 12.75, 17.0 and 21.25 m/s, respectively. The bubble Reynolds number, based on the air injecting velocity (u_g) and the nozzle inner diameter, was in the range of 574~7179 (see Table 1). The bubble flow was illuminated by two halogen lamps and a high-speed CMOS camera (Photron Fastcam SA2/86K-M3) fitted with a Nikon lens (45 mm f/2.8D) was used to capture bubble images. The resolution of the camera was set as 2048 × 2048 pixels. For each case, the camera recorded over 5400 bubble images and its sampling rate was listed in Table 1. The magnification of the bubble image was 0.19 mm/pixel resulting in a field of view (FOV) equalling about 390 mm × 390 mm, as the dashed square shown in Figure 1 (a). Figure 1 (c) presented an image snapshot of real bubble flow. It can be seen that the bubbles could be clearly distinguished from the background flow. Based on some image processing methods, further quantitative information of bubbles could be obtained, which would be explained in detail in the following sections.

For the current experimental arrangements, one would expect a development of a boundary layer over the flat plate. Hence, a two-dimensional time-resolved particle image velocimetry (TR-PIV)

system was used to accurately acquire the incoming flow conditions for the bubble flow, including the boundary layer information as well as the free-stream velocity. The PIV system, which has been used by Xu & Wang [17] and Xu et al. [18], contained a continuous laser with power of 5W, a high-speed CMOS camera (same with bubble image), a Macro lens (Nikon 105 mm f/2.8D) and a personal computer. The laser sheet, with thickness of about 1.0 mm, was parallel to the streamwise direction and crossed the centreline of the nozzle (see Figure 1 (b)). Additionally, since the purpose of the PIV experiment was to validate the incoming flow, the nozzle was placed at the edge of the laser sheet, as shown in figure 1(b). Hollow glass beads with a median diameter of 10 μm and density of 1.05 g/cm³ were employed as seeding particles. In order to store more images, the resolution of the camera was set as 1536 \times 1792 pixels leading to a FOV of 129 mm \times 149 mm in streamwise and wall-normal directions, respectively. For each free-stream velocity case, 8315 particle images were recorded and they were analysed by a multi-pass interrogation algorithm with the final interrogation window equalling 32 \times 32 pixels. With a 75% overlap, the vector space of the velocity field was about 0.67 mm for both streamwise and wall-normal directions. Using 0.1 pixels as the uncertainty of subpixel peak fitting, the uncertainty of the PIV measured velocity was estimated to be less than 1 %.

2.2 Incoming flow condition.

Based on above PIV measurements, Table 2 summarized both the free-stream velocity and the boundary layer information for all the tested cases. It can be seen that five free-stream velocities (U_∞) resulted in friction (Re_τ) and momentum (Re_θ) Reynolds numbers in the range of 218–841 and 388–2177 respectively for this experiment. Furthermore, Figure 2a gives the mean streamwise velocity profile of $U^+(y^+)$ for all the cases. The classical log-law of $U^+ = \frac{1}{\kappa} \ln(y^+) + B$ (black solid line) was also plotted for comparison with constants $\kappa = 0.41$ and $B = 5.0$. From figure 2(a), it can be seen that for all the tested free-stream velocities, the boundary layer over the flat plate could be treated as full-developed turbulence before interacting with the nozzle, which was used to generate bubbles. In particular, Table 2 shows that the boundary layer thickness (δ) for all the cases was larger than the nozzle height (28 mm) indicating that the nozzle was submerged in the boundary layer. Thus, the bubble injected from the nozzle exit should suffer from a high shear rate, which might have some influences on the bubble characteristics. Based on the velocity profile in Figure 2 (a), a nominal mean shear rate is presented in Figure 2 (b) for all the free-stream velocity cases. Here, the nominal shear rate was obtained by calculating the spatial gradient of the mean streamwise velocity ($\partial U / \partial y$) at a wall-normal position equalling the nozzle height. As shown in Figure 2 (b), the mean shear rate was increased with the growth of the free-stream velocity. This indicated that for the same air flow rate, the bubble at a higher free-stream velocity would experience a larger flow shear stress. Specially, the mean shear rate for the largest free-stream velocity ($U_\infty = 334$ mm/s) was about nine times as much as that for the smallest ($U_\infty = 58.5$ mm/s).

2.3 Image analysis

To analyse flow characteristics of bubble swarms in the cross-flow condition, we developed a novel high-speed image-processing method which can extract flow data from the high-speed photographs. The analysis is non-intrusive and flow properties (such as velocity, bubble size) can be obtained everywhere in the Field of View (FOV). Before extracting data from images, a series of image processing steps were taken to convert raw images to refined binary images suitable for digital feature extraction of bubble properties. This procedure includes (1) background subtraction, (2) thresholding and filtering, (3) edge detection, (4) edge dilatation, (5) filling holes and (6) edge erosion process. Background subtraction is a process to clarify the bubble flows in the FOV. Subtracting background image with bubble images, pixels which are occupied by bubble can be remained but, backgrounds are removed. However, it is not necessary process if bubble images have clear bubble edges. The background image subtraction can be represented with the following expression:

$$I(x, y) = I_B(x, y) - I_O(x, y) \quad (1)$$

where I , I_B , I_O are processed image, background image, and original image respectively. Thresholding operation is necessary as it allows bubbles outside the camera's focus depth to be blurred by Gaussian smoothing. This way, once images are edge detected, the blurred out-of-focus bubbles are not recognised. Figure 3 (b) shows the edge-detected for the given sample. It is an essential process to find bubbles' outline using the grayscale gradient of pixels. While the elimination of out-of-focus bubbles is not perfect, we observe that it provides slightly less error than without this operation after analysis for void fraction. Comparison of velocity results for with and without discarding out of focus bubbles shows that there is no significant difference between, even though thresholding and filtering add additional processing steps and result in increased processing time for the entire dataset. For edge detection, the Prewitt method was adopted, from which conversion to binary images was possible. The method has the benefit of computational speed with horizontal and vertical mask but, but it has a weakness regarding diagonal detection. Thus, detected outline is not completely closed and there could be blanks between some bubble edges. To complement diagonal detection, there is need to conduct an edge dilation process which expands edges in four directions. In order to do this for the current study, an algorithm was implemented thus:

$$I_{dil,x}(x, y) = \begin{cases} 1, & I(x-1, y) = 1 \\ 1, & I(x+1, y) = 1 \\ 0, & \text{else} \end{cases} \quad (2a)$$

$$I_{dil,y}(x, y) = \begin{cases} 1, & I(x, y-1) = 1 \\ 1, & I(x, y+1) = 1 \\ 0, & \text{else} \end{cases} \quad (2b)$$

$$I_{dil}(x, y) = I(x, y) + I_{dil,x}(x, y) + I_{dil,y}(x, y)$$

$$I_{dill}(x, y) = \begin{cases} 0, & I_{dill}(x, y) = 0 \\ 1, & I_{dill}(x, y) > 0 \end{cases} \quad (2c)$$

where $I_{dil,x}$, $I_{dil,y}$ are dilated images toward x and y direction respectively and I_{dill} is dilated image toward both x and y direction. Bubble filling follows edge dilation and this is implemented by replacing all pixels within the completed bubble boundary with unit values (Figure 3 (d)). Enlarged bubble sizes are created by image dilation and this is visually clear by comparing Figure 3 (a) and (d). Hence, an edge eroding process should follow such that additional layers created during dilation are eroded. This is easily implemented using the Matlab function “imerode”. Eroded images have the same bubble sizes with those in the original image (Figure 3 (e)).

2.4 Bubble trajectory angle and velocity profile determination

Obtaining bubble trajectories is important in crossflows. While this allows the validation of any systematic assessment of the balance of influential forces, such as drag, the trajectory can facilitate the determination of characteristic rise velocities of the bubbles. For these reasons, the trajectory is determined by obtaining the mean centroid of all bubbles in the binary image along a horizontal axis at any vertical position. Connecting this with the nozzle exit provides a convenient way of obtaining the trajectory assuming the bubbles motion is quasilinear as previously observed [6]–[8]. An example is shown in Figure 4 at $Q_g = 10$ L/min. Each of the images selected randomly, shows that the mean line of trajectory is representative of the entire sample.

Characteristic rise velocities are obtained from the images at different vertical positions. In this study, three vertical positions were used midpoint through three regions vertically partitioned to be of equal size and referred here to as “bottom”, “middle”, and “top” regions (first image in Figure 4). To determine the characteristic velocities at these three locations, a two-signal data extraction method was implemented. On each region in the binary image, we place two points, above and below, along a line parallel to the line of bubble trajectory (Figure 5 a). From these two points, we can extract a series of zeros (water, black) and ones (bubble, white) from each image and construct two time series as shown in Figure 5 (b). From these, we then calculate characteristic time lags (τ) between the two time series analogous to signals obtained by a physical sensor. A pair of bubble signals can have many time lags (e.g. τ_1 , τ_2 , τ_3 ...) which are not necessarily the same. Therefore, a representative (or most probable) time lag between upper signal (U) and bottom signal (B) is calculated. This is done by calculating the sliding inner-product (*) of the upper and bottom signals as follows:

$$(U * B)(\tau) = \int_{k=-\infty}^{k=\infty} [U(k)][B(k + \tau)]dt \quad (3)$$

Equation (3) applies to continuous valued functions. However, for discrete signals such ours, we calculate a cross-correlation function $R_{T,B}(k)$ to find the most corresponsive time lag between the two signals:

$$R_{U,B}(k) = \sum_{k=1}^N [U(k) - \bar{U}][B(k + \tau) - \bar{B}] \quad (4)$$

where \bar{U} and \bar{B} are the mean values of the respective signal time series. When $R_{T,B}$ has the maximum value, the most corresponsive time lag at that position is τ_{max} . From this, we can calculate the characteristic bubble velocity at a point since we specified the gap between upper and bottom extraction points; i.e.:

$$u_b = \frac{y}{\tau_{max}} \quad (5)$$

The vertical gap between two points y , is carefully selected by sensitivity analysis since bubble velocity can be dramatically altered with a small difference in τ_{max} .

The horizontal gap between two points (x) is calculated as follows:

$$x = \frac{y}{\tan\theta} \quad (6)$$

A series of extraction points is positioned on the binary image to calculate velocity along the bubble trajectory. For the three vertical positions chosen (see Figure 6), these give velocity profiles with which we can examine the velocity evolution as the bubbles rise towards the surface. Extraction points are horizontally positioned at 94.5, 188.9 and 283.4 mm from the bottom of images.

Tiny bubbles at the fringes of the swarm can give rise erroneous or infinite velocities due to their zigzag motion which allows them to escape detection points. Hence, a valid range has to be set to exclude such bubbles some of which are only a few pixels in size. Already collected time series signal can be used to calculate the bubbles void fraction, α_b , which can in turn be used to define a valid spatial range for the velocity profile. In order to decide this valid range, a criteria based on the cumulative distribution function (CDF) of $\alpha_{valid,i}$ is used:

$$\beta_{valid,i} = \begin{cases} 0 & \alpha_{valid,i} \in CDF(\alpha_{valid,i}) < 0.1 \\ 1 & \alpha_{valid,i} \in 0.1 \leq CDF(\alpha_{valid,i}) \leq 0.9 \\ 0 & \alpha_{valid,i} \in CDF(\alpha_{valid,i}) > 0.9 \end{cases} \quad (7)$$

$$where, \quad \alpha_{valid,i} = \frac{1}{T} \sum_{j=1}^M \Delta t_j \quad (j = 1, 2, \dots)$$

where M is the number of bubbles passing the i th pixel; and Δt is the time for the j th bubble to have stayed on the pixel. The vector $\beta_{valid,i}$ of unit valued elements which can be used as weighting to determine the velocity profile “valid spatial range”. Indeed, the span of the red and blue crosses in

Figure 6 was determined this way. The bubble velocity calculated in each pixel at an angle to the bubble trajectory is within the valid extraction range is as follows:

$$u_{b,j} = \frac{y_j}{\tau_{max,j}} \quad (j = 1, 2, 3 \dots N) \quad (8)$$

where N is the pixel length within the valid extraction range. To determine a representative velocity for each Q_g and U_∞ combination, we used only the velocities within the profile that were outside one standard deviation from the minimum velocity within that profile. This method using the standard deviation ensures that even highly skewed velocity profiles do not produce biased means. This is depicted in Figure 7. As shown in the figure, there could be sudden changes of velocity in the right side of velocity profile. Especially, edges of velocity profile have relatively small amount of void fraction. It means velocity profile at edge is not from sufficient signal samples and there might be noise such as lateral motion of bubbles. So, it is not smoothly distributed over the x axis. Therefore, velocity from relatively small void fraction regions are not reliable, they can result in a lower than realistic mean, and should be neglected. The criteria for neglecting these areas of the velocity profile for the purpose of determining the mean bubble velocity is based on only selecting velocities that are higher than one standard deviation from the minimum void fraction. Hence spatial locations with sparse bubble concentration are carry a weighing value $w_{b,j}$ of zero and otherwise they are assigned a value of unity; i.e.:

$$w_{b,j} = \begin{cases} 0 & \alpha_{b,j} < \alpha_{b,min} + \sigma_\alpha \\ 0 & \alpha_{b,j} < \alpha_{b,min} + \sigma_\alpha \\ 1 & else \end{cases} \quad (9)$$

where σ_α is one standard deviation of the magnitude of void fraction values. Therefore, the mean velocity calculated after selecting a valid range is obtained as follows:

$$u_{b,mean} = \frac{\sum_{i=1}^N w_{b,i} u_{b,i} \alpha_{b,j}}{\sum_{i=1}^N w_{b,i} \alpha_{b,j}} \quad (10)$$

As will be shown in section 3, the procedure of Equations (7)–(10) leads to stabilised mean bubble (rise and streamwise) velocities, and vary predictably according to the systematically varied prevailing experimental conditions. Focus is placed on points with frequently passing bubbles hence the reducing bias introduced by low bubble count, meandering bubbles, and profile skew.

To recap, standard deviation is needed to neglect small bubbles in high free stream velocity conditions where the void fraction profile is skewed. In such a case, standard deviation increases because the void fraction is not evenly distributed. However, in low freestream cases or even the quiescent conditions, standard deviation is not sufficient to neglect small bubbles. So, the CDF should be used, since their motion could be irregular and miss both detection points, hence leading to unreliable data. When we use the CDF criterion, we can neglect a fixed portion of the void fraction regardless of

its spatial distribution. But, if the CDF criterion is so strict, even large bubbles' information could be neglected in high freestream velocity case. Therefore, we used both criteria, CDF and standard deviation, to determine valid spatial ranges for the velocity profile in each case.

3 Results and discussion

3.1.1 Validation

Before being used for further analysis, it is important to validate the velocity here obtained and hence the image processing method used. Previously, Aliyu et al. [19] compared the rise velocities of single bubbles in still water obtained using a dual optical fibre probe (OFP) with that obtained using images captured with a high-speed camera acquired at 8,000 fps. They reported that rise velocities at inlet gas flows of 1–5 L/min gas flow between the two methods were within $\pm 2\%$ of each other. Alcan et al. [20] and Kiambi et al. [21] also obtained rise velocities for bubbles of 2–4 mm mean diameter using image processing techniques. The former developed a method to track the evolution of low Reynolds number bubbles in jet flow. While their method was capable of tracking bubbles in real time, large morphological changes in bubble shape (such as in this study) can result in high unreliability in the method. Conversely, Kiambi et al. compared image processing results with measurements using OFPs. They obtained values that were in good agreement with a $\pm 5\%$ mean difference between both methods. In order to validate the velocity measurements made here, comparison was made with the experimental results of Kiambi et al. [21] who used a combined particle image/tracking velocimetry (PIV/PTV) method to measure the velocity of bubbles generated in quiescent liquid conditions. Air was ejected using 14-mm diameter submerged nozzle in a water tank. They used a high-speed camera to obtain images containing both bubbles and fluid tracer particles and grey-scale thresholded, phase-separated images of the bubbles were produced. Bubble velocities were obtained from the images using PTV. A standard PIV method was used on the mixed fluid images, and bubble vectors are removed using a velocity threshold and vector median filter that is calibrated to the PTV result. Their time-averaged velocities followed a top-hat profile shape that is best fitted with a curve proposed by Monkewitz [22] to describe shallow water wake profiles. The Monkewitz curve is as follows:

$$u(x, y) = \frac{u_{b,max}(y)}{1 + \sinh^{2\gamma}(x/p)} \quad (11)$$

where $u_{b,max}(y)$ is the maximum or centreline bubble swarm velocity at vertical position y , p is the width of the bubble swarm, all obtained from the mean velocity fields; and γ is a “shape parameter” that modifies the flatness of the top part of the profile. A value of $\gamma = 3$ was found to better suit the mean bubble profiles. As shown in Figure 8, there is a good match between our experimental velocity profile and those of Seol et al. [23] at 1.5 L/min. Although the figures show that our velocities were slightly higher than both their PIV and PTV values, it is because their larger nozzle size will produce lower gas velocities in the nozzle. This in turn translates to lower bubble rise velocities in the liquid.

Nevertheless, the agreement is noted and this gave us confidence that our measurement method produces acceptable results. There are of course obvious error sources such as out of plane bubbles motion as well as wobbly trajectories by the small and trailing bubbles within the measurement plane. However, triplicate measurements showed that measured velocities were within a maximum of $\pm 10\%$ of each other, with the mean deviation being in the neighbourhood of $\pm 5\%$.

3.2 Bubbles visualisation

Images of all 36 experiments of submerged bubbles under quiescent and crossflow conditions are shown in Figure 9. As can be seen, for all freestream velocities, bubble size increases with an increase in gas flow rate Q_g . This is evident by visual observation when moving from 2 to 5 L/min or from 10 to 15 L/min for example. At low freestream flows, bubbles are mostly spherical immediately after detachment from the nozzle but these become increasingly non-spherical with increase in the freestream velocity. The latter shapes can best be described as irregular ellipsoids skewed towards the direction of flow. In all cases however, upon rising through the fluid, all bubbles morph into irregularly shaped ellipsoids with the creation of much smaller trailing bubbles especially at large Q_g . One interesting feature at large freestream velocities is the advanced forward position of the smaller bubbles. Their lower masses and hence lower momentum results in the apparent ease with which they are transported with the crossflowing liquid compared to the larger ones.

At the initial stage of bubble detachment from the nozzle the swarm momentum dominates over the crossflow drag. This is more so because, we calculated that the crossflow velocity profile near the nozzle exit is still within the boundary layer. On rising further, the bubbles' trajectory bends slightly due to the decaying momentum of the swarm and the increasing influence exerted by the crossflow as the velocity increases from the boundary layer to the freestream. Afterwards, the smaller bubbles are seen to start separating from the swarm meaning a slip exists between the freestream and the core of the swarm's centroid.

Figure 9 shows that overall, the angle of the gas bubbles centreline trajectory increases slightly with increase in Q_g . In the 36 experimental conditions, ranging from around 7° from the vertical plane for all the $U_\infty = 0.059$ m/s cases to between 40° and 46° in the $U_\infty = 0.334$ m/s cases. For all conditions studied, the bubble swarms appear to travel in pseudo-linear trajectories. The superimposed red continuous lines in the figure are trajectories obtained as the mean centroid of the swarm in all 5,000 images for each flow case. Each image in Figure 9 was randomly selected from the set of 5,000, thereby demonstrating the accuracy of the image processing procedure. Furthermore, the blue dashed lines were predicted using a correlational curve fit of the experimental trajectories and dimensionless numbers characterising the gas and liquid properties and flow conditions. Details are presented in subsequent paragraphs.

Similar behaviour of the swarm trajectories we observed has been previously reported [6]–[8] and is said to be controlled by the vector sum of the surrounding streamwise velocity, slip, and the buoyancy-induced rise velocity. This is represented by the summation [24]:

$$\vec{u}_b = \vec{U}_s + \vec{U} + \vec{U}_{bw} \quad (12)$$

where \vec{U} is the vector sum of ambient velocity, \vec{U}_s is the slip velocity, \vec{U}_{bw} is the bubble-induced water velocity (see Figure 10). The slip velocity is directly calculated using the drift-flux relationship of Clift et al. [25]:

$$U_s = \sqrt{\frac{2.14\sigma}{\rho d_b} + 0.505gd_b} \text{ for } d_b > 1.3 \text{ mm} \quad (13)$$

where σ , ρ_l and g are surface tension between air and water, density of water, and gravitational acceleration respectively. From Figure 10, it is clear that $\theta' = \tan^{-1}(\vec{U}_s/\vec{U}_\infty)$ or $\theta' = \cos^{-1}(\vec{U}_s/u_b)$ assuming \vec{U}_{bw} negligible. However, in their study, Zhang & Zhu [24] observed that the former method of determining θ' predicts values quite close to those obtained from the high-speed images. Conversely, the latter method using the inverse cosine overestimates θ' by as much as 23% when compared with those from the images for larger bubbles. This suggests that \vec{U}_{bw} is not negligible and can be as much as 0.012 m/s when bubbles reach 7 mm in size. In such cases, the swarm induces high turbulence within the liquid crossflow. For the current experiments, basic image processing was applied to obtain the angle using the tangent method and θ is subsequently calculated:

$$\theta = 90 - \theta' = 90 - \tan^{-1}(y/x) \quad (14)$$

where y and x are the lengths of the vectors \vec{U}_s and \vec{U}_∞ easily determined from the swarm mean centroid determined from the images. For each case 5,000 images was used and overall, deviations from the mean value of θ were less than 5%.

Numerous researchers have worked on predicting single-phase jet trajectories in crossflows with some of the earliest studies being those of Pratte & Baines [26], Wright [27], and Hodgson & Rajaratnam [28] amongst others. For most of these studies, the jet centreline trajectory was predicted using various versions of a model first proposed by Wright [27]. It consists of two parts, the momentum dominated near field (MDNF) model, and the momentum dominated far field (MDFF) model, given as follows respectively:

$$\begin{aligned} \text{In MDNF where } y \leq l_m \quad \frac{y}{Rd} &= \left(1.88 - \frac{2.07}{R^{2/3}}\right) \left(\frac{x}{Rd}\right)^{1/2} \\ \text{In MDFF where } y > l_m \quad \frac{y}{Rd} &= (0.82R^{1/6}) \left(\frac{x}{Rd}\right)^{1/2} \end{aligned} \quad (15)$$

where $R = u_g/U_\infty$ is the ratio of bubble jet velocity at the nozzle exit; x and y are the streamwise and vertical distance from the nozzle respectively; and $l_m = M_o^{1/2}/U_\infty$ is a dimensionless length scale with M_o being the specific momentum flux (u_g^2) at the nozzle exit. We tested the model equations against

our experimental results and obtained satisfactory predictions at high gas flow rates where the turbulent jet is likely to take a linear or quasilinear trajectory. Significant deviations occurred between the model and our data at lower bubbling rates where in their work, produced parabolic trajectories. We note that the MDNF and MDFF models have been successfully applied to buoyant plumes where the exit fluid is two-phase. In such cases, excellent agreement with experimental data was achieved (see [28], [29]); the trajectories in especially the liquid have been shown to be parabolic particularly near the nozzle exit but for the gas phase, on getting to the far field region, quasi-linear trajectories are followed.

Therefore, it is necessary to have a prediction method for the current bubble swarms, which consists of single-phase plumes, and follow essentially linear trajectories. In order to produce such a relation, a correlational approach shall be adopted. The mean inclination angle can be expressed as a function of the freestream velocity, gas flow rate, and other important variables. Here, we select 9 main parameters as follows:

$$\theta = f(U_\infty, u_g, d_{noz}, \rho_g, \rho_l, \sigma, \mu_g, \mu_l, d_{ch,H}) \quad (16)$$

where $u_g = Q_g / (\frac{\pi d_{noz}^2}{4})$ the gas velocity in the nozzle; d_{noz} is the nozzle diameter; $\rho_g, \rho_l, \mu_g, \mu_l, \sigma$ and $d_{ch,H}$ are the gas and liquid densities and viscosities, air–water surface tension and channel height under consideration respectively. Buckingham's Pi theorem allows us to determine the number of dimensionless (or Π) groups that can be determined from Equation (16) and in this case since we have 9 variables, $\Pi = 9 - k = 6$ where $k = 3$ is the number of fundamental dimensions of mass, length, and time. Therefore, the number of dimensionless groups is 6. If we select U_∞, ρ_l , and $d_{ch,H}$ as the repeating variables, the other six nonrepeating variables are distributed to construct the six Π -groups as follows:

$$\begin{aligned} \pi_1: & U_\infty, \rho_l, d_{ch,H}, \mu_l \\ \pi_2: & U_\infty, \rho_l, d_{ch,H}, \mu_g \\ \pi_3: & U_\infty, \rho_l, d_{ch,H}, \sigma \\ \pi_4: & U_\infty, \rho_l, d_{ch,H}, d_{noz} \\ \pi_5: & U_\infty, \rho_l, d_{ch,H}, \rho_g \\ \pi_6: & U_\infty, \rho_l, d_{ch,H}, u_g \end{aligned}$$

Using, dimensional analysis, the dimensionless numbers are easily deduced from the variables as $\pi_1 = \frac{\rho_l U_\infty d_{ch,H}}{\mu_l} = Re_\infty$, the freestream Reynolds number; $\pi_2 = \frac{\rho_l U_\infty d_{ch,H}}{\mu_g} = Re_*$, a characteristic Reynolds number; $\pi_3 = \frac{\rho_l U_\infty^2 d_{ch,H}}{\sigma} = We_\infty$, the freestream Weber number; $\pi_4 = \frac{d_{noz}}{d_{ch,H}}$; $\pi_5 = \frac{\rho_g}{\rho_l}$; and $\pi_6 = \frac{u_g}{U_\infty}$. We note that π_2 as a Reynolds number is physically meaningless, it contains a mixture of gas and liquid variables. Multiplying it by π_4, π_5 , and π_6 , we obtain $\pi_2' = \frac{\rho_g u_g d_{noz}}{\mu_g} = Re_g$, the gas Reynolds number. The following groupings are hence arrived at for the determination of θ :

$$\theta = f(Re_{\infty}, Re_g, We_{\infty}) = K Re_{\infty}^a Re_g^b We_{\infty}^c \quad (17)$$

where K , a , b , and c are constants of the power law curve to be determined by regression. The Reynolds numbers capture the inertia of the flowing fluids and the Weber number characterises the ability of the crossflowing liquid to cause bubble breakup since it is a balance of inertial to surface tension forces. While the number of dimensionless groupings is reduced to three, it is not exhaustive. Other dimensionless groups may be relevant in describing the flow trajectory, but their inclusion will only make using the correlation a bit more cumbersome without necessarily resulting in commensurate increase in accuracy. Fitting Equation (17) to the current experimental data with a power law curve using multiple nonlinear least-squares regression yields an expression for predicting the swarm trajectory θ :

$$\theta = 0.03 \frac{Re_{\infty}^{0.63} We_{\infty}^{0.15}}{Re_g^{0.14}} \quad (18)$$

Figure 11 (a) shows that Equation (18) fits the swarm displacement trajectory for all the conditions tested and the predictions were sufficiently collapsed to $\pm 15\%$ of the experimental values in most cases. It shows that θ has a direct proportionality with the freestream Reynolds number, while it varies inversely with the gas Reynolds number. These are physically consistent with the observations in Figure 9 since increase in gas flow and hence momentum will continually dominate at constant freestream flow. Furthermore, the trajectory varies proportionally with the freestream Weber number. Increase in this dimensionless number results in the production of smaller bubbles as will be shown in the next section (since We_{∞} is mostly affected by the freestream velocity U_{∞}). Figure 11 (b) clearly shows these qualitative trends as well as good quantitative agreement between the predicted and experimental trajectories. It should be noted that this correlation is applicable within the bounds of the current experimental conditions and for water–air systems only. Further validation will be needed for other conditions and fluid physical properties, or better still, a mechanistic model should be derived that applies regardless of fluid combination or physical properties.

3.3 Bubble size distribution

Bubbles in the refined binary image were statistically analysed by aid of Matlab's image processing tools. Bubble number and pixelated area of each bubble were acquired from bubble binary images. The bubble area is calculated as the number of pixels comprising each object, i.e.

$$A_{b,i} = \iint p(x,y) dx dy = \sum p(x_v, y_h) \quad (19)$$

where p is the pixel at position (x, y) , the subscripts v , and h denote vertical and horizontal pixel counters respectively. The pixels are summed over the area covered by the bubble in question. An area equivalent bubble diameter is calculated for every bubble in the frame as:

$$d_{b,i} = \sqrt{\frac{4A_{b,i}}{\pi}} \quad (20)$$

shows size distributions that were constructed for $Q_g = 10$ and 20 L/min. It can be seen that the distributions initially have two peaks at still water conditions and at low crossflows (Figure 12). As the crossflow velocity increases, the second peak with the higher bubble size begins to move leftwards indicating the production of smaller bubbles (indicated by the arrows). This suggests that increasing liquid crossflow promotes bubble breakup. At the highest crossflow velocities of $U_\infty = 0.231$ and 0.334 , the distributions are distinctly single peaked at less than 0.5 mm in diameter. The average diameter was calculated using a volumetric average as follows:

$$d_{b,v} = \left[\frac{\sum (n_i d_{b,i}^3)}{\sum n_i} \right]^{\frac{1}{3}} \quad (21)$$

where $d_{b,i}$ is the bubble diameter of the i th group and n_i is the number of bubbles with a diameter of $d_{b,i}$. Some authors have used this volume averaging method [30]. Others utilised a Sauter mean diameter [31], [32] but where there is large size variation, it can result in averages biased towards larger bubbles. Therefore, the volume averaged bubble diameter was taken as the more acceptable value here since it was more consistent with the observations of the distributions in Figure 12. Table 3 shows the mean bubble diameter calculated using the volume average in Equation (12). It can be seen that the mean bubble velocities increase with increasing Q_g but are suppressed with increasing crossflow velocity at the same gas flow rate. The latter agrees with the observations as illustrated in the size distributions in **Error! Reference source not found.** Figure 12 where increasing crossflow velocity causes a shift from two peaks to one peak in favour of the smaller bubble sizes. Again, this is a clear indication of the incoming momentum of the crossflowing liquid resulting in the breakup of the rising bubbles.

3.4 Prediction of swarm rise velocity under crossflow

Figure 13**Error! Reference source not found.** shows the relationship between the bubble swarm rise velocity and crossflow freestream velocity at different inlet air flow rates. The current experimental data were plotted alongside those of Wang & Socolofsky [33] obtained at $Q_g = 0.004 - 0.096$ L/min and $U_\infty = 0.02 - 0.15$ m/s. As can be seen, the current data obtained at much higher gas and crossflow velocities produced higher bubble rise velocities. These rapidly decrease with increase in crossflow velocity at all inlet gas flow rates. At high crossflows, the rise velocities seem to asymptote towards the terminal velocity of a single bubble in quiescent flow, represented by the dashed blue line. In order to obtain a correlation that describe these trends, it is pertinent to revisit the works of previous researchers carried out for single bubbles and swarms in still water conditions as well as for low gas flow swarms and low liquid crossflows.

For the prediction of bubble rise velocities in quiescent flow, Marks [34] found out that the velocities can be satisfactorily predicted using a dimensional relationship which is a function of the inlet gas flow rate only, i.e.:

$$u_b = 18.1Q_g^{0.141} \quad (22)$$

where u_b is in cm/s and Q_g in cm³/min. Figure 14 shows that this equation is remarkably consistent with our measured bubble velocities in still water. However, deviations begin to occur with increasing crossflow velocity, which is expected since the correlation does not account for this parameter. It is therefore necessary to introduce the effect of the crossflow to accurately model the rise velocity. Attempts have been made in the past to do this, which we briefly present in the following paragraphs.

Wang & Socolofsky [33] tested the correlation against their experimental data and also reported its accuracy at quiescent water conditions especially at gas flow rates higher than 20 ml/min. To account for other parameters such as the wake effect of leading bubbles and bubbles mixing length, Marks [34] further derived a dimensionless relationship using the turbulent wake theory.:

$$\left(\frac{u_b}{u_{b,T}}\right)^{5/3} - \left(\frac{u_b}{u_{b,T}}\right)^{2/3} = K \left(\frac{12gQ_g^2}{\pi\beta^2 u_{b,T}^4 d_b^3}\right)^{1/3} \quad (23)$$

where K is a proportionality constant, β is a coefficient related to the ratio of the bubbles mixing length to the half-width of the wake region as defined by Schlichting [35]. In their paper, Wang & Socolofsky [33] showed that for ellipsoidal bubbles within the diameter range of 0.8–10 mm, Equation (23) can be expressed as the following, which greatly collapses their rise velocity data:

$$\frac{u_b}{u_{b,T}} - 1 = K \left(\frac{gQ_g^2}{u_{b,T}^4 d_b^3}\right)^{1/3} \quad (24)$$

where K was found to be 1.5. This equation formed the basis of their analysis for obtaining a relationship for rise velocity under crossflows where they reasoned that K cannot be constant in crossflows. They observed that the slopes of the best fit regression lines for the different bubble velocities in each crossflow condition followed the simple exponential relation given by

$$s = \exp(-0.3U_\infty) \quad (25)$$

Wang & Socolofsky [33] now replaced K in Equation (24) with s and arrived at the correlation

$$\frac{u_b}{u_{b,T}} - 1 = \exp(-0.3U_\infty) \left(\frac{gQ_g^2}{u_{b,T}^4 d_b^3}\right)^{1/3} \quad (26)$$

Equation (26) remarkably collapsed their data with a high correlation coefficient. In order to apply this relationship to our rise velocities, it is clear that a relationship for s has to be obtained that fits the current data since it is evident in Figure 13 that the slopes of u_b against U_∞ decays more slowly at high gas flows. Hence for the current experiments, $s = 0.54\exp(-2.36U_\infty)$ was found to give the best fit.

Substituting this instead of Equation (22) and curve-fitting to the data, we can rewrite the dimensionless model for the swarm rise velocities in crossflows as follows:

$$\frac{u_b}{u_{b,T}} - 0.72 = 0.45 \exp(-2.36 U_\infty) \left(\frac{g Q_g^2}{u_{b,T}^4 d_b^3} \right)^{1/3} \quad (27)$$

The correlation is plotted alongside the experimental data in **Error! Reference source not found.** with an R^2 value of 0.85. Despite the presence of some scatter, this represents satisfactory performance with many of the points being within $\pm 20\%$ of the curve. The scatter could be because the slopes do not sufficiently decay with the limited crossflow conditions of our experiments, and these could hence form the basis of a future study. Also for future study, the spreading behaviour of the bubbles as well as the effect of the turbulent wake in crossflow should be considered. Under crossflow conditions, it has been suggested that the trailing bubbles are located at some offset distance from the centreline leading to a reduction of the wake influence on the rise velocity. This needs to be thoroughly investigated theoretically. Furthermore, since correlations are only valid within the range of their data or experimental conditions, a physical model based on force balances is necessary. Such a model, would be comprised of simplified momentum and continuity equations with the balance of buoyancy, drag, virtual mass force, etc. being the source terms. The bubble size distributions experimentally determined here can be fed into the numerical solution of the model as closure. While such numerical or analytical models are important in initial designs of aeration systems, and studying underwater gas pipe leakages, experimental studies such as the current are valuable in providing data to calibrate computational fluid dynamics models.

4 Conclusions

Experiments were carried out in a small water channel to study the effect of crossflow velocity on rising bubble plumes over a wide range of gas flow rates. High-speed bubble visualisation was done and in the still water condition, bubbles were observed to be initially spherical upon detachment from the nozzle, but deform into ellipsoids and spherical cap bubbles on rising towards the free surface and more so as the gas bubbling rate increases since drag forces through the liquid increase. Under crossflow however, the bubbles could best be described as irregularly shaped ellipsoids skewed towards the direction of flow. On rising through the fluid, there was the creation of much smaller trailing bubbles especially at large gas flow rates. These resulted in dually modal bubble size distributions which were damped with increasing liquid crossflow due to bubble break up induced by rising viscous drag forces. Using a specially written image processing algorithm, we extracted quantitative information on trajectories, size distribution, rise velocities of the bubble swarm. Rise trajectories are essentially linear and are heavily influenced by the crossflow. We initially tested the momentum dominated near and far field correlations first proposed by Wright but these failed to adequately predict our trajectories. We conclude that there is a limit to which their equations apply which may have an upper limit of bubbling

rate as this significantly affects the shape of the trajectory. In their studies parabolic trajectories were reported, as against the quasilinear observed here. Using dimensional analysis, we derived a correlation in terms of the gas capillary, Froude and freestream Reynolds numbers that very well predicts the swarm trajectory. Increasing crossflow was found to severely suppress the swarm rise velocity which decay asymptotically towards the terminal velocity of a single bubble rising in quiescent water. This observation was consistent with that of other authors who used more limited gas and crossflow velocities than the current experiments. Using the correlating scheme of Marks derived from the turbulent wake theory, as modified by Wang & Socolofsky, we obtained a relationship for the dimensionless bubble rise velocity as a function of the liquid crossflow velocity and gas bubbling rate.

Acknowledgement

This work was also supported by the National Research Foundation of Korea (NRF) grant funded by the Korean government (MSIP) through GCRC-SOP (No. 2011-0030013). We also acknowledge the funding provided by the BK21 Plus Program of the School of Mechanical Engineering, Pusan National University, Republic of Korea.

Nomenclature

A. Roman

Ca	[-]	Capillary number
d	[m]	diameter
Fr	[-]	Froude number
I	[pixels]	Image intensity
p	[-]	Swarm width
Q	[L/min or m ³ /s]	Volumetric flow rate
Re	[-]	Reynolds number
u	[m/s]	Velocity specified by a subscript
x	[m]	Horizontal spatial coordinate
y	[m]	Vertical spatial coordinate

B. Greek

α	[-]	Void fraction
γ	[-]	Velocity profile shape parameter
κ	[-]	Von Karman constant
μ	[kg/s-m]	Dynamic viscosity
ρ	[kg/m ³]	Density
σ	[N/m]	Liquid surface tension
θ	[°]	Swarm angle of inclination or trajectory (for linear and quasi linear swarms)
τ	[s]	Cross-correlation time lag

C. Subscripts

b	bubble
-----	--------

g	Gas phase
l	Liquid phase
noz	Nozzle
s	Slip, used for slip velocity
sg	Superficial gas
T	Terminal
τ	Shear as used with Re and u for the crossflow liquid
∞	freestream

References

- [1] A. K. Ghosh and J. J. Ulbrecht, "Bubble formation from a sparger in polymer solutions—II. Moving liquid," *Chem. Eng. Sci.*, vol. 44, no. 4, pp. 969–977, 1989.
- [2] M. H. Jobehdar, K. Siddiqui, A. H. Gadallah, and W. A. Chishty, "Bubble formation process from a novel nozzle design in liquid cross-flow," *Int. J. Heat Fluid Flow*, vol. 61, no. 2, pp. 599–609, Oct. 2016.
- [3] K. Loubiere, V. Castaignede, G. Hebrard, and M. Roustan, "Bubble formation at a flexible orifice with liquid cross-flow," *Chem. Eng. Process. Process Intensif.*, vol. 43, no. 6, pp. 717–725, 2004.
- [4] R. B. H. Tan, W. B. Chen, and K. H. Tan, "A non-spherical model for bubble formation with liquid cross- flow," *Chem. Eng. Sci.*, vol. 55, no. July, pp. 6259–6267, 2000.
- [5] S. E. Forrester and C. D. Rielly, "Bubble formation from cylindrical, flat and concave sections exposed to a strong liquid cross-flow," *Chem. Eng. Sci.*, vol. 53, no. 8, pp. 1517–1527, 1998.
- [6] R. Manasseh, S. Yoshida, and N. Kajio, "Bubble Trajectory Bifurcations in Cross Flow," in *Proceedings of 13th Australasian Fluid Mechanics Conference*, 1998, p. 1013.
- [7] S. A. Socolofsky and E. E. Adams, "Multi-phase plumes in uniform and stratified crossflow," *J. Hydraul. Res.*, vol. 40, no. 6, pp. 661–672, Nov. 2002.
- [8] W. Zhang and D. Z. Zhu, "Bubble characteristics of air – water bubbly jets in crossflow," *Int. J. Multiph. Flow*, vol. 55, pp. 156–171, 2013.
- [9] J. H. Milgram, "Mean flow in round bubble plumes," *J. Fluid Mech.*, vol. 133, no. 1, p. 345, Aug. 1983.
- [10] A. Wüest, N. H. Brooks, and D. M. Imboden, "Bubble plume modeling for lake restoration," *Water Resour. Res.*, vol. 28, no. 12, pp. 3235–3250, Dec. 1992.
- [11] S. A. Socolofsky, T. Bhaumik, and D.-G. Seol, "Double-plume integral models for near-field mixing in multiphase plumes," *J. Hydraul. Eng.*, vol. 134, no. 6, pp. 772–783, 2008.
- [12] I. E. Lima Neto, "Modeling the Liquid Volume Flux in Bubbly Jets Using a Simple Integral Approach," *J. Hydraul. Eng.*, vol. 138, no. February, pp. 210–215, 2012.
- [13] T. Y. Sun and G. M. Faeth, "Structure of turbulent bubbly jets-II. Phase property profiles," *Int. J. Multiph. Flow*, vol. 12, no. 1, pp. 115–126, 1986.
- [14] M. T. Dhotre, B. Niceno, B. L. Smith, and M. Simiano, "Large-eddy simulation (LES) of the

- large scale bubble plume,” *Chem. Eng. Sci.*, vol. 64, no. 11, pp. 2692–2704, Jun. 2009.
- [15] A. Esmaeeli and G. Tryggvason, “Direct numerical simulations of bubbly flows. Part 1. Low Reynolds number arrays,” *J. Fluid Mech.*, vol. 377, p. S0022112098003176, Dec. 1998.
- [16] A. Esmaeeli and G. Tryggvason, “Direct numerical simulations of bubbly flows Part 2. Moderate Reynolds number arrays,” *J. Fluid Mech.*, vol. 385, p. S0022112099004310, Apr. 1999.
- [17] Y. Xu and J. J. Wang, “Flow structure evolution for laminar vortex rings impinging onto a fixed solid wall,” *Exp. Therm. Fluid Sci.*, vol. 75, pp. 211–219, Jul. 2016.
- [18] Y. Xu, G. He, V. Kulkarni, and J. Wang, “Experimental investigation of influence of Reynolds number on synthetic jet vortex rings impinging onto a solid wall,” *Exp. Fluids*, vol. 58, no. 1, p. 6, Jan. 2017.
- [19] A. M. Aliyu, Y. K. Kim, S. H. Choi, J. H. Ahn, and K. C. Kim, “Development of a dual optical fiber probe for the hydrodynamic investigation of a horizontal annular drive gas/liquid ejector,” *Flow Meas. Instrum.*, vol. 56, pp. 45–55, Aug. 2017.
- [20] G. Alcan, M. Ghorbani, A. Kosar, and M. Unel, “A new visual tracking method for the analysis and characterization of jet flow,” *Flow Meas. Instrum.*, vol. 51, pp. 55–67, Oct. 2016.
- [21] S. L. Kiambi, A.-M. Duquenne, J.-B. Dupont, C. Colin, F. Risso, and H. Delmas, “Measurements of Bubble Characteristics: Comparison Between Double Optical Probe and Imaging,” *Can. J. Chem. Eng.*, vol. 81, no. 3–4, pp. 764–770, 2003.
- [22] P. A. Monkewitz, “The absolute and convective nature of instability in two-dimensional wakes at low Reynolds numbers,” *Phys. Fluids*, vol. 31, no. 5, p. 999, 1988.
- [23] D. Seol, T. Bhaumik, C. Bergmann, and S. A. Socolofsky, “Particle Image Velocimetry Measurements of the Mean Flow Characteristics in a Bubble Plume,” *J. Eng. Mech.*, vol. 133, no. 6, pp. 665–676, Jun. 2007.
- [24] W. Zhang and D. Z. Zhu, “Trajectories of Air-Water Bubbly Jets in Crossflows,” *J. Hydraul. Eng.*, vol. 140, no. 7, p. 6014011, Jul. 2014.
- [25] R. Clift, J. R. Grace, and M. E. Weber, *Bubbles, drops, and particles*. New York: Academic Press, 1978.
- [26] B. D. Pratte and W. D. Baines, “Profiles of the round turbulent jets in a cross flow,” *ASCE J. Hydraul. Div.*, vol. 93, no. 6, pp. 53–64, 1967.
- [27] S. Wright, “Mean behavior of buoyant jets in a crossflow,” *ASCE J. Hydraul. Div.*, vol. 103, no. 5, pp. 499–513, 1977.
- [28] J. E. Hodgson and N. Rajaratnam, “An experimental study of jet dilution in crossflows,” *Can. J. Civ. Eng.*, vol. 19, no. 5, pp. 733–743, Oct. 1992.
- [29] W. Zhang, “Air injection for river water quality improvement,” University of Alberta, 2012.
- [30] J. Yin, J. Li, H. Li, W. Liu, and D. Wang, “Experimental study on the bubble generation characteristics for an venturi type bubble generator,” *Int. J. Heat Mass Transf.*, vol. 91, pp. 218–

- 224, 2015.
- [31] S. Zheng, Y. Yao, F. Guo, R. Bi, and J. Li, "Local bubble size distribution, gas–liquid interfacial areas and gas holdups in an up-flow ejector," *Chem. Eng. Sci.*, vol. 65, no. 18, pp. 5264–5271, Sep. 2010.
- [32] A. Gordiychuk, M. Svanera, S. Benini, and P. Poesio, "Size distribution and Sauter mean diameter of micro bubbles for a Venturi type bubble generator," *Exp. Therm. Fluid Sci.*, vol. 70, pp. 51–60, 2016.
- [33] B. Wang and S. A. Socolofsky, "On the bubble rise velocity of a continually released bubble chain in still water and with crossflow," *Phys. Fluids*, vol. 27, no. 10, 2015.
- [34] C. H. Marks, "Measurements of the terminal velocity of bubbles rising in a chain," *J. Fluids Eng.*, vol. 95, pp. 17–22, 1973.
- [35] H. Schlichting, *Boundary-Layer Theory*. New York: McGraw-Hill, 1979.

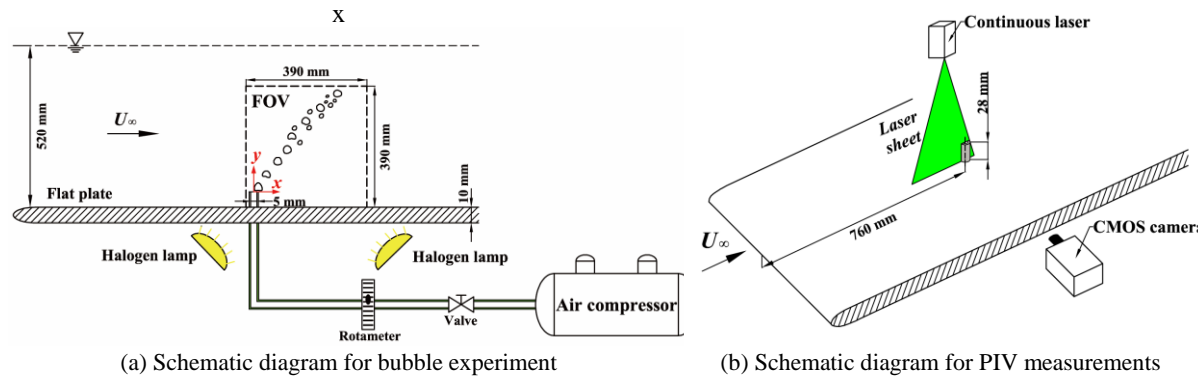


Figure 1: Overall experimental setup.

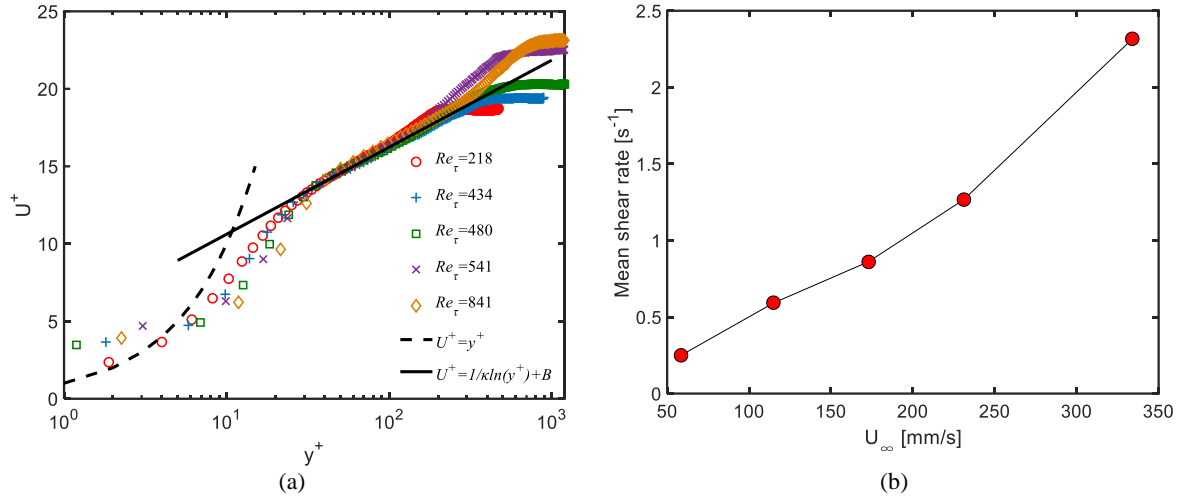


Figure 2: (a) Profiles of ensemble-averaged streamwise velocity $U^+(y^+)$ for all the free-stream velocity cases from PIV measurements, where log-law constants of $U^+ = \frac{1}{\kappa} \ln(y^+) + B$ are $\kappa = 0.41$ and $B = 5.0$. (b) Nominal mean shear rate ($\partial U / \partial y$) at a wall-normal position equalling the nozzle height for all the cases

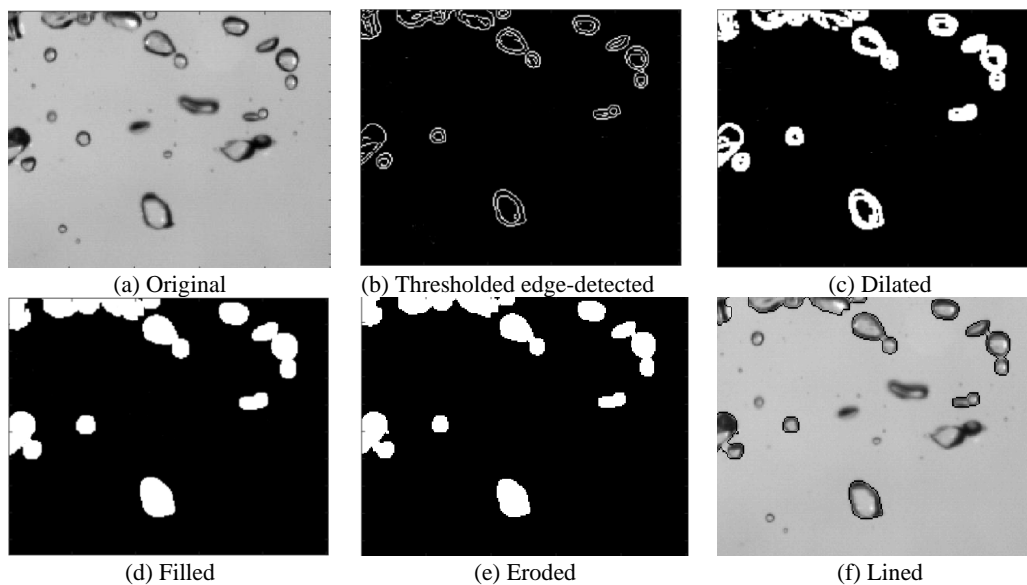


Figure 3: digital image processing steps

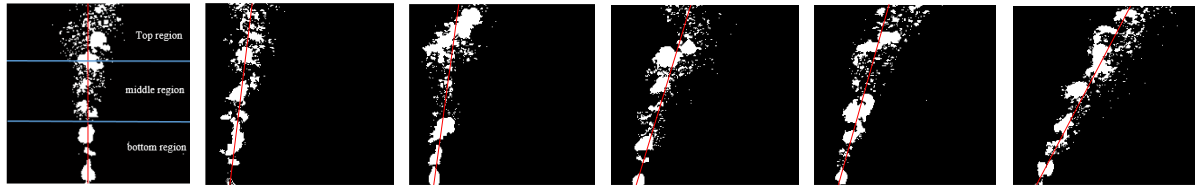
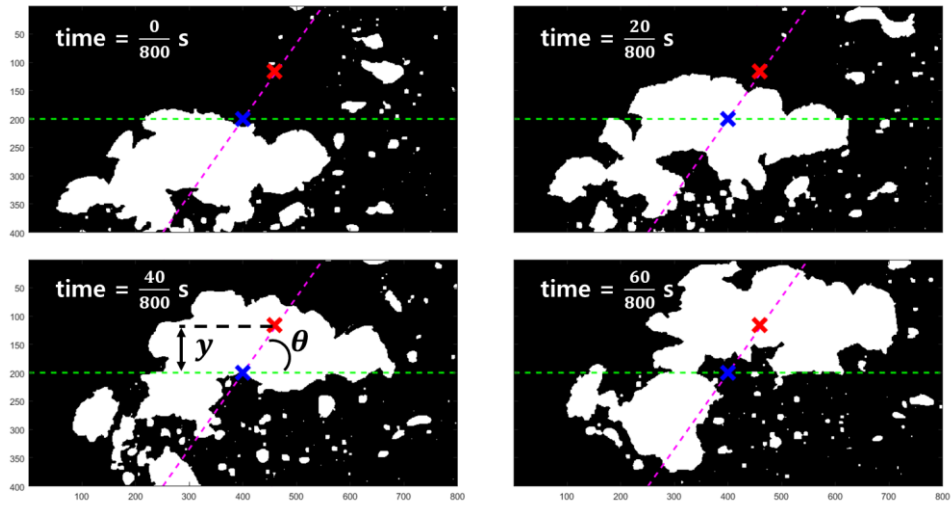
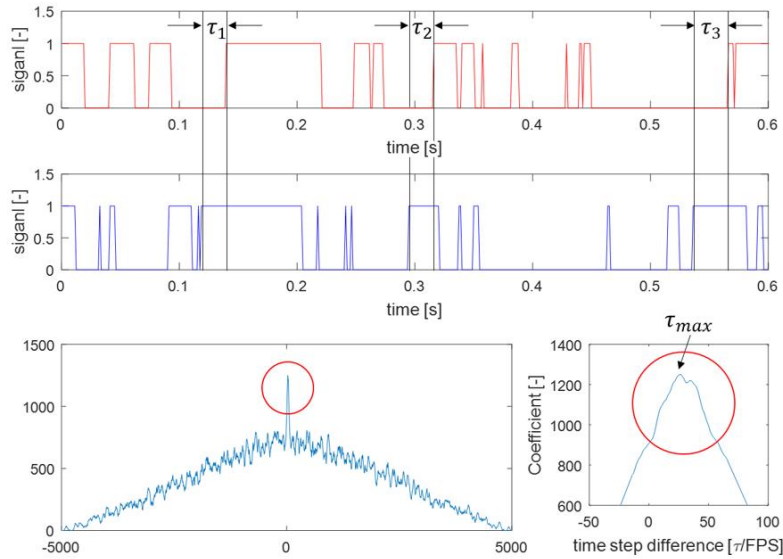


Figure 4: Bubbles angle of inclination from processed images at 10 L/min. Left to right $U_{\infty} = 0, 0.059, 0.115, 0.173, 0.231, 0.334$ m/s



(a)



(b)

Figure 5: bubble velocity determination (a) snapshots showing data extraction points on line parallel to line of trajectory (b) upper and bottom time series and cross-correlation function

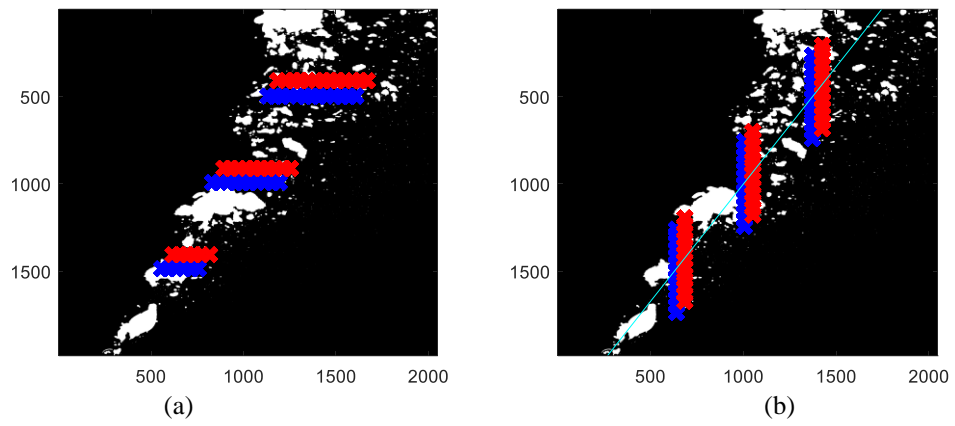
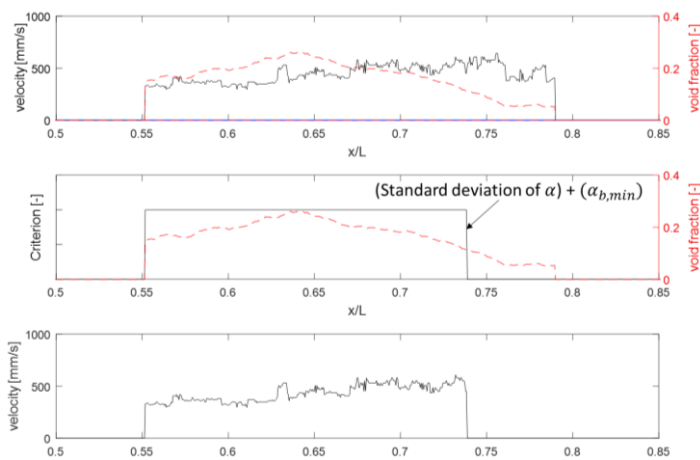


Figure 6: Schematic for data extraction points to construct (a) rise, and (b) streamwise velocity profiles

625



626 **Figure 7: determination of a valid spatial range for velocity profile using the bubble void fraction**

627

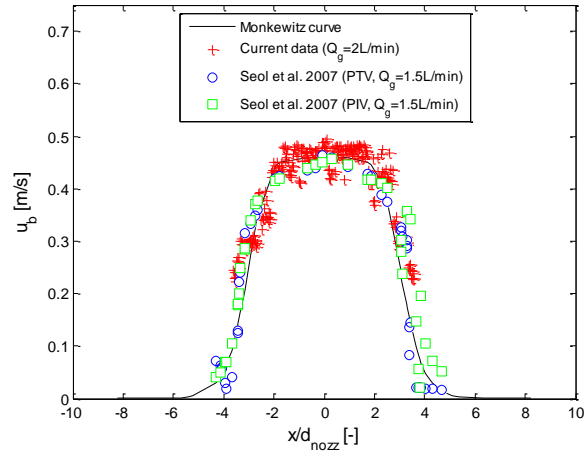


Figure 8: Comparison of current velocity profile at $Q_g = 2$ L/min with the PTV and PIV data of Seol et al. [23] as well as a Monkewitz curve.

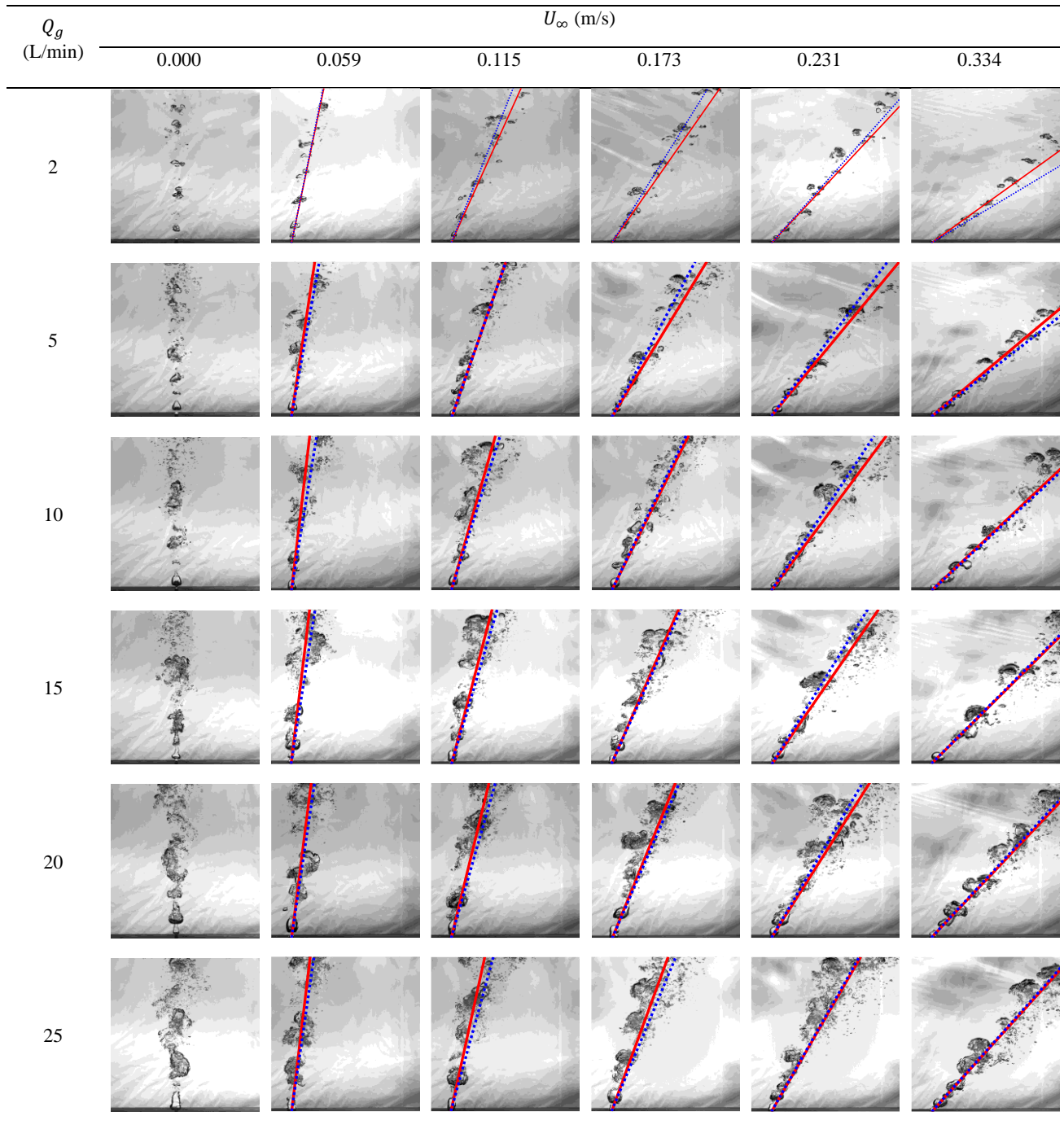


Figure 9: High-speed visualisation of bubbles under different gas flow crossflow conditions. Red continuous lines represent the experimental trajectories obtained as mean swarm centroid in all images. Blue dashed lines are predictions using Equation (18)

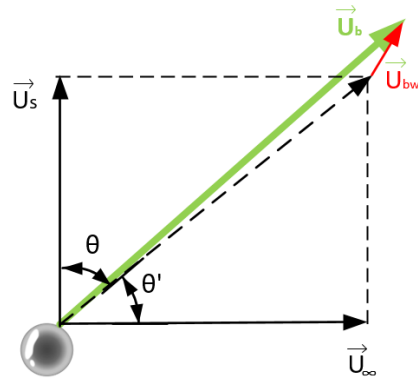
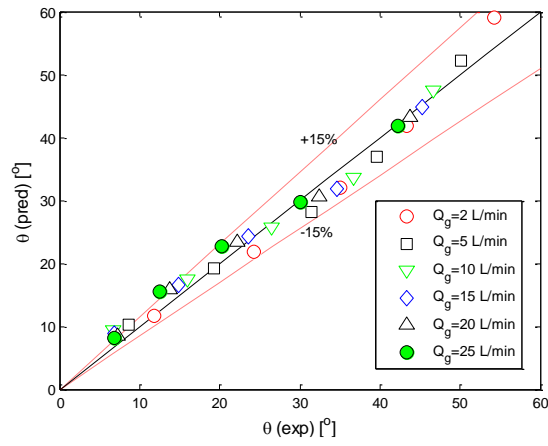
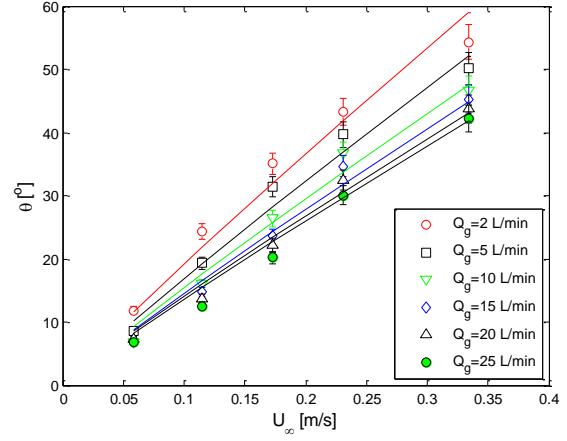


Figure 10: Velocity vectors associated with a bubble in liquid crossflow (adapted from Zhang & Zhu [24])

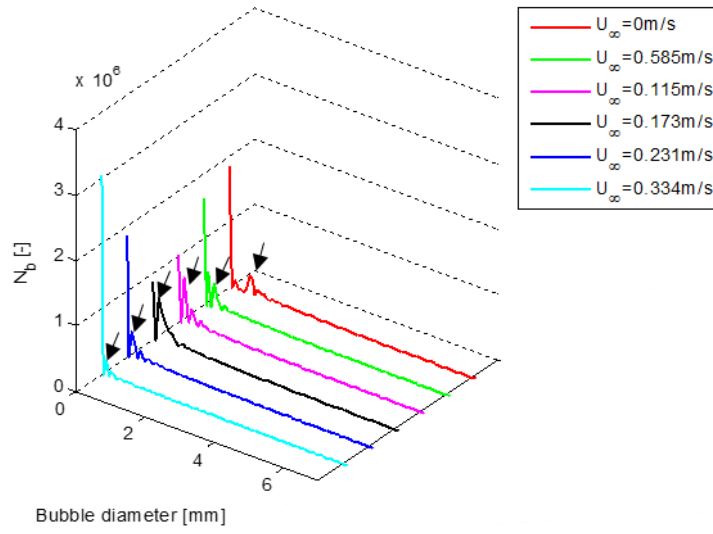


(a)

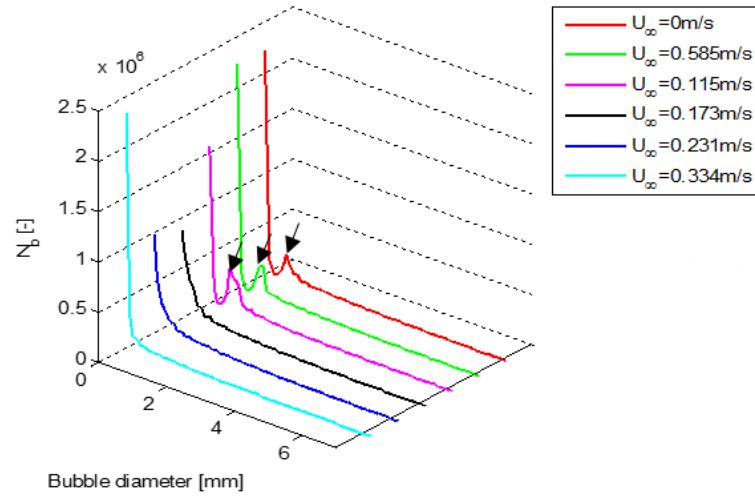


(b)

Figure 11: Graphical representation of Equation (18) (a) parity plot showing error band (b) Effect of freestream velocity on mean swarm inclination angle: experimental data points vs predictions



(a)



(b)

Figure 12: Representative bubble size distributions showing effect of freestream velocity (Shown here are for (a) $Q_g = 10$ L/min and (b) 20 L/min). Where N_b is the number of bubbles.

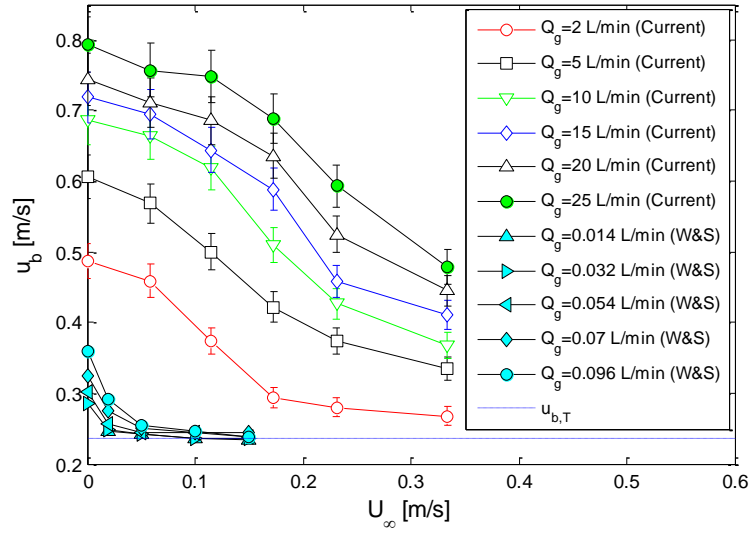


Figure 13: Mean bubble rise velocities under crossflow. The error bars represent the average deviation between three measurements. W&S are the data of Wang & Socolofsky [33], and $u_{b,T}$ (represented by the blue dashed line) is the terminal velocity for a single bubble rising in quiescent water.

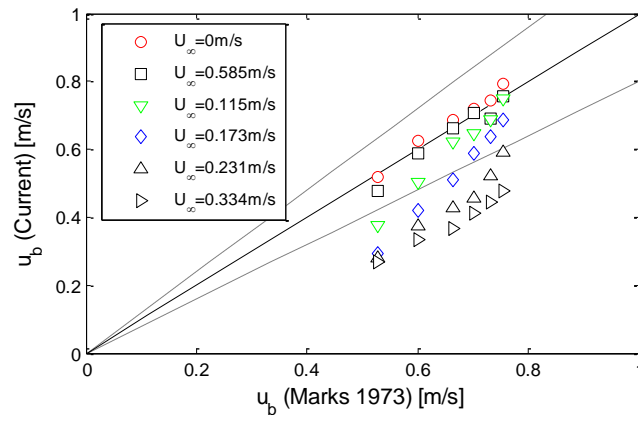


Figure 14: Comparison of current bubble velocities with the prediction of Marks [34] Eq. (22).

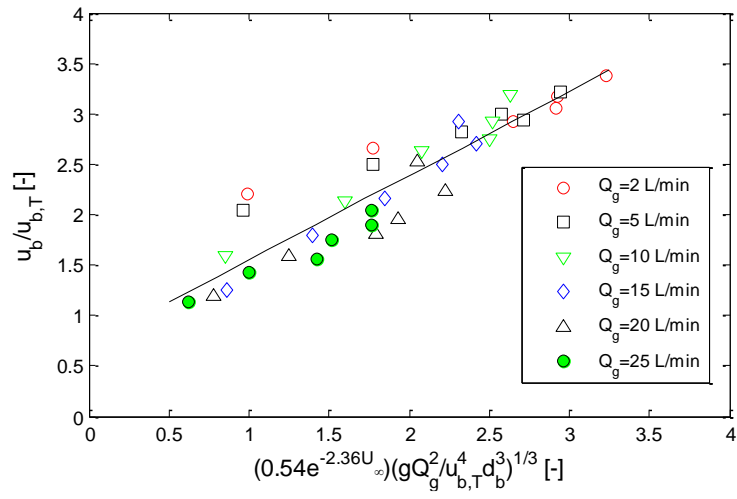


Figure 15: Correlation for dimensionless bubble swarm rise velocity